Nitrogen-doped graphene flakes/dots /Fe₃N as oxygen reduction reaction electrocatalyst

Rui Yan[1,2], Huinian Zhang[1,2], Congwei Wang[1], Yongzhi Liu[1], Quangui Guo[1], Junzhong Wang[1]*

[1]*CAS Key Laboratory of Carbon Materials, Institute of Coal Chemistry, Chinese Academy of Sciences, Taiyuan, 030001, P R China*
[2]*University of Chinese Academy of Sciences, Beijing 100049, PR China*

*Corresponding author. Tel: (+86) 0351 4040407; E-mail: wangjz@sxicc.ac.cn

Abstract

Nitrogen-doped graphene flakes/dots/Fe₃N hybrids were synthesized by electrochemical charging/discharging of graphite in ionic liquid/water followed by thermal annealing at the presence of FeCl₃. Rich edges of graphene dots and porous graphene flakes from electrochemical etching probably supply heteroatom-doping sites and active catalytic sites while porous graphene flakes support good electrical conductivity and pathway for electrons/ions/gases. The graphene flakes/dots/Fe₃N material obtained at 700 °C shows the highest oxygen reduction reaction (ORR) activity with half-wave potential of 753 mV (vs RHE) and better durability and tolerance of methanol than Pt/C. Copyright © 2017 VBRI Press.

Keywords: Graphene, electrocatalyt, oxygen reduction reaction, nitrogen doping.

Introduction

Efficient catalysts for the oxygen reduction reaction (ORR) are considered the key to achieve superior performance for fuel cells and metal-air batteries [1, 2]. Pt-based precious metals have been known as the most efficient ORR catalysts [3-6]. However, the high price, sluggish ORR process, intolerance to fuel crossover, and instability of the Pt/C catalyst in fuel-cell environment have greatly impeded the commercialization of fuel cells and limited their practical applications [7]. To solve these problems, numerous efforts have been devoted to the development of nonprecious metals [8, 9] and even metal-free ORR catalysts[10, 11].

Recent researches have demonstrated that introducing transition metals, especially Fe, into the nitrogen-doped nanocarbon framework to form Fe-N/C catalyst can generate strong synergistic catalysis for ORR, resulting a novel non-PGM catalyst system with improved electrocatalytic performance [12-15]. However, finely tuning the active electrolytic sites at a low cost is still challenging. Here, we report an approach to prepare porous graphene flakes/dots/Fe₃N composite for ORR electrocatalyst. This approach involves electrochemical charging/discharging of graphite in ionic liquid followed by annealing at the presence of FeCl₃.

The synthesis process involves one-pot charging/discharging to intercalate/expand each graphite electrode to prepare graphene, etching the graphene flakes into graphene dots and porous graphene in ionic liquid/water firstly, and then followed annealing after adding FeCl₃. The carbonating of ionic liquid not only provides a source of nitrogen doping but prevents the restacking of graphene. The resulting G/dots/Fe₃N composite highlights the abundant Fe-N active sites, tunable N content, mesoporous microstructure and excellent electrical conductivity. Such unique material features not only provide a large amount of active sites for efficient ORR, but also are favorable for the fast transport of oxygen and reduction products. As a consequence, G/dots/Fe₃N (700ºC) exhibit good ORR electrocatalytic properties, including high electrocatalytic activity, long-term durability and high selectivity.

Experimental

Materials

1-butyl-3-methylimidazolium tetrafluoroborate was purchased from Linzhou Keneng Material Technology CO., LTD. Commercial 20 wt. % Pt/C catalyst and 5 wt. % Nafion solution were purchased from Shanghai Hesen Electric CO., LTD. Other chemicals, such as FeCl₃· 6H₂O and ethanol were bought from China Medicine Shanghai Chemical Reagent Corp. All reagents were analytically pure and used as received without further purification.

Materials preparation

The electrochemical preparation of the precursor was performed in an electrolyte solution of water and ionic liquid (IL) of 1-butyl-3-methylimidazolium tetrafluoroborate ([BMIM][BF₄]). Briefly, graphite papers were used as both negative and positive electrodes. The electrodes were immersed into the solution of IL/water (1/1, v/v) with a distance of 3.0 cm. Static potential of 5 V was applied to the two electrodes, with the exchange of

current direction in every eight hours. After three days, the electrolyte solution was centrifuged to obtain the mixture. Then the product mixture with ethanol (30 mL) was sonicated for one hour and then dried overnight at 80 ℃. 0.7 g of the dried mixture was then redispersed in 20 mL of ethanol under stirring followed by ultrasound. Next, different amounts of $FeCl_3 \cdot 6H_2O$ (25, 35, and 70 mg) were added into the above dispersion under vigorous stirring. The Fe content of the corresponding products was 6.8%, 11.54%, and 15.26%, respectively, according to the inductively coupled plasma (ICP) measurements. Finally, the mixture was pyrolyzed at 600, 700, 800, 900 ℃ at a heating rate of 10 ℃min^{-1} for 30 min under nitrogen flow to obtain the catalyst materials.

Characterization

Scanning electron microscopy (SEM) images were obtained on a field emission scanning electron microscopy JSM-7001F (FESEM). Transmission electron microscopy (TEM) images were obtained with JEM-2100F microscope at an acceleration voltage of 200 kV. X-ray powder diffraction (XRD) was recorded at a scan rate of 0.02°/s using the Cu Kα (1.540600 Å) line. X-ray photoelectron spectroscopy (XPS) measurements were performed using Thermo ESCALAB 250 spectrometer, employing an Al-KR X-ray source with a 500 μm electron beam spot. Raman data were measured in Jobin-Yvon HR-800 Raman system with 532 nm line of Ar laser as excitation source. Thermal analysis (TG/DTA) was carried out using a thermal analyzer (Netzsch STA409PC) at a heating rate of 10 ℃ /min from 20 to 800 ℃. The pore size distribution and Brunauer-Emmett-Teller (BET) specific surface area were deduced from the N_2 physical adsorption measurement data that were obtained using an ASAP 2010 Accelerated Surface Area and Porosimetry System.

Electrochemical tests

A glassy carbon (GC) electrode was carefully polished with gamma alumina powder. Then the electrode was rinsed and fully sonicated with distilled water to remove alumina residues. Finally, it was dried in vacuum. In a mixture of 5% Nafion (10 μL) and ethanol (1 mL), the catalysts (4 mg) were dispersed by sonication. Then, the dispersion (20 μL) was drop-casted onto the GC electrode surface (diameter 5 mm). A platinum wire was used as the

counter electrode and Ag/AgCl electrode as the reference electrode. All the experiments were conducted at room temperature, in an O_2 or N_2-saturated 0.1 M KOH aqueous solution. Cyclic voltammetry (CV) measurement and rotating disk electrode (RDE) voltammetry were all performed using an Autolab electrochemical analyzer and a MSR electrode rotator (PINE, USA) at different rotation rates. The scanning rate is 50 mV/s for the CV measurements, and 10 mV s^{-1} with various rotating speeds for the LSV measurements.

Prior to ORR measurements, the solution was bubbled with O_2 for 30 min. The transferred electron numbers per oxygen molecule involved in the ORR were determined using the Koutechy-Levich (K-L) equation:

$$\frac{1}{J} = \frac{1}{J_k} + \frac{1}{B\omega^{1/2}}$$

where, J is the measured current density, J_k are the kinetic- and diffusion-limiting current densities, B is the Levich constant, and ω is the electrode rotating rate. The transferred electron numbers per oxygen molecule can be calculated from the Levich constant as follows:

$$B = 0.62nFD^{2/3}V^{-1/6}c_0$$

where, n is the transferred electron numbers per oxygen molecule, F is the Faraday constant ($F = 96485$ Cmol^{-1}), D is the diffusion coefficient of O_2 in 0.1 M KOH (i.e., 1.9×10^{-5} cm^{2}s^{-1}), V is the kinetic viscosity (0.01 cm^{2}s^{-1}), and C_0 is the bulk concentration of oxygen (i.e., 1.2×10^{-3} molL^{-1}).

Results and discussion

The synthetic process of the G/dots/Fe$_3$X composite is illustrated in **Scheme 1**. Firstly, the electrochemical preparation of the precursor was performed in an electrolyte solution of water and ionic liquid (IL) of 1-butyl-3-methylimidazolium tetrafluoroborate ([BMIM][BF$_4$]). During the charging/discharging at high potential, graphite was exfoliated, and resulting graphene flakes were partially etched into graphene dots and porous graphene nanomeshes. The electrolytic products contain

Scheme 1. Illustration of synthesis of porous graphene flakes/dots/iron compounds (G/dots/Fe₃X).

graphite   Graphene dots   Fe₃X
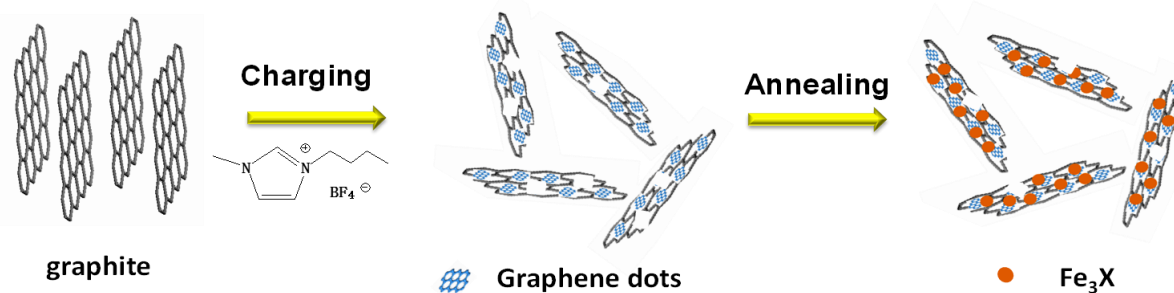
graphene quantum dots, porous graphene flakes and intercalated IL. Then $FeCl_3$ was mixed with the electrolytic products and carbonized at various temperatures to obtain G/dots/Fe_3X, where x represents carbonization temperature of 600, 700, 800, and 900 °C. As a control, G/dots are prepared by carbonizing the electrolytic products at 600-900 °C without Fe source. IL mixing $FeCl_3$ was also carbonized at 700 °C, denoted as C/Fe_3N.

Fig. 1a shows the XRD patterns of the pyrolyzed composites synthesized at different temperatures with the same Fe content of 11.54%. The sharp and relatively strong peak at 26.5° corresponds to the (002) graphitic plane of graphene, indicating the high graphitization degree. The XRD pattern of the composite (700 °C) shows a distinct peak at 43.7°, which is significantly different from other samples. This peak is attributed to the fingerprint peak of Fe_3N (JCPDS number 49-1664). When the pyrolysis temperature was increased to 800 °C, Fe_3C (JCPDS number 65-0393) peaks can be detected. As presented in Fig. S1b, all of the samples pyrolyzed at 700 °C with different Fe contents show the peaks of Fe_3N, which indicated that Fe_3N phase could be produced at 700 °C. If the Fe content was reduced to 6.8%, the peak of Fe_3O_4 phase appeared.
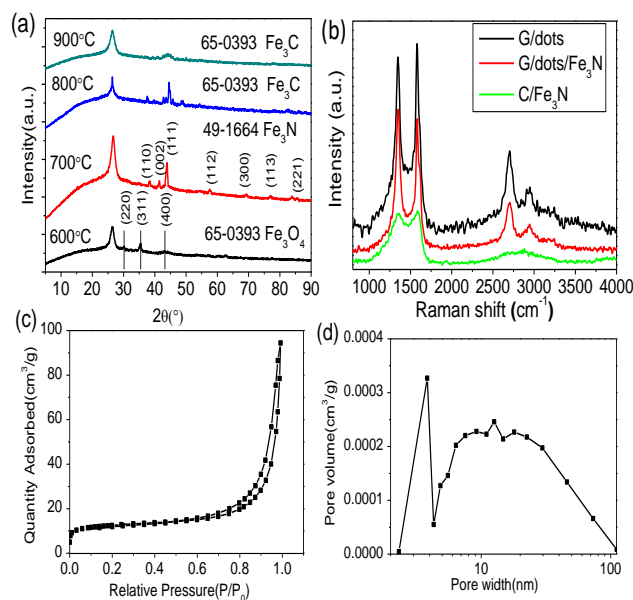
Fig. 1. (a) XRD patterns of graphene flakes/dots/iron compounds samples obtained under different calcination conditions; (b) Raman spectra of G/dots, G/dots/Fe_3N and C/Fe_3N, (c) BET surface area and (d) pore size distribution of G/dots/Fe_3N (700 °C).

If the Fe content was increased to 15.26%, Fe_3C was formed. There seemed be a competition between the formation of Fe_3C and Fe_3N. Pyrolyzing at 700 °C with 11.54% content of Fe was the optimum condition to form Fe_3N. **Fig. 1c** and **d** show the nitrogen adsorption/desorption isotherm curve and pore size distribution of graphene flakes/dots/Fe_3N (700°C). The BET surface area was 43.2 m²g⁻¹, and the pore-size distribution presented a sharp peak around 2 nm and a large broad peak from 3 to 100 nm, indicating the mesoporous microstructure features of the catalyst (**Fig. 1c and d**). The pore size distribution was

corresponding to the size of the graphene dots and the pores of porous graphene nanomeshes.

TEM imaging can clearly observe the graphene dots and porous graphene nanomeshes, as shown in **Fig. 2.** Crystal lattices of graphene can be clearly presented, which indicated of high quality of graphene dots and nanomeshes.
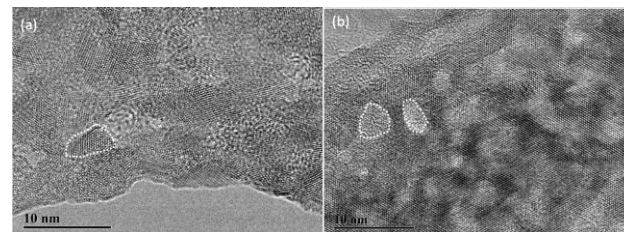

Fig. 2. (a, b) High resolution TEM images of graphene quantum dots and porous graphene flake.

The size of graphene quantum dots (3-4 nm) is consistent with the pore size of porous graphene. After annealing at 700°C at the presence of $FeCl_3$, the black powder product of G/dots/Fe_3N was analyzed by TEM accordingly. Low-magnification SEM and TEM images demonstrated crumpled sheet-like morphology with coarse surface, as shown in Fig. 3a,b. High resolution TEM image presents the nanoparticles of dots/Fe_3N (**Fig. 3c, d**). **Fig. 3d** exhibited ~5 nm size of Fe_3N nanoparticles. The electron diffraction pattern (**Fig. 3e**) reflected the co-existence of Fe_3N and graphene
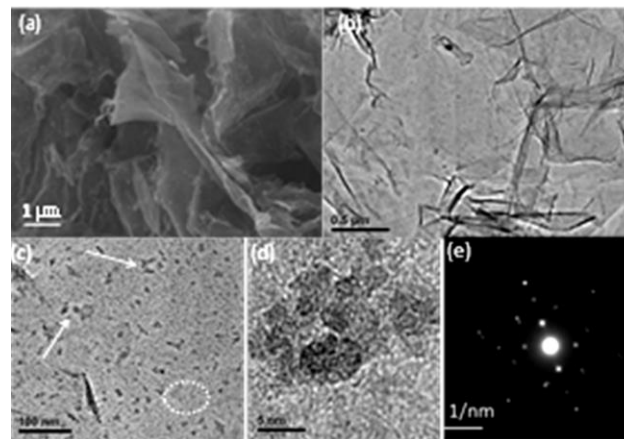

Fig. 3. (a) SEM image, (b) TEM images of graphene quantum dots and porous graphene; (c，d) TEM images of G/dots/Fe_3N (700 °C); (e) The selected area electron diffraction pattern of G/dots/Fe_3N (700 °C).

The chemical composition of G/dots/Fe_3X was evaluated by XPS. The full XPS spectrum (**Fig. 4a**) revealed that the as-prepared G/dots/Fe_3X consisted of C, N, O, and Fe featured peaks, indicating that N and Fe have been successfully doped into the material. The content of N was calculated as 5.3, 4.7, 3.5 atomic percentage at different annealing temperatures, respectively (**Table 1**).

The peaks in N1s spectra of all samples (panels b-d of **Fig. 4**) can be divided into three N species: pyridinic N (N1, 397-399 eV), quaternary N (N2, 401-403 eV) and oxidized N species (N3, 404-405 eV), in which pyridinic

N (397-399 eV) can coordinate with Fe in the form of Fe-Nx. In this work, N1 (398.6 ± 0.3 eV) can be regarded as N atom that bonds to doped iron metal atom (Fe-Nx); while oxidized N species do not significantly contribute to the ORR performance and are unstable under fuel cell working conditions.
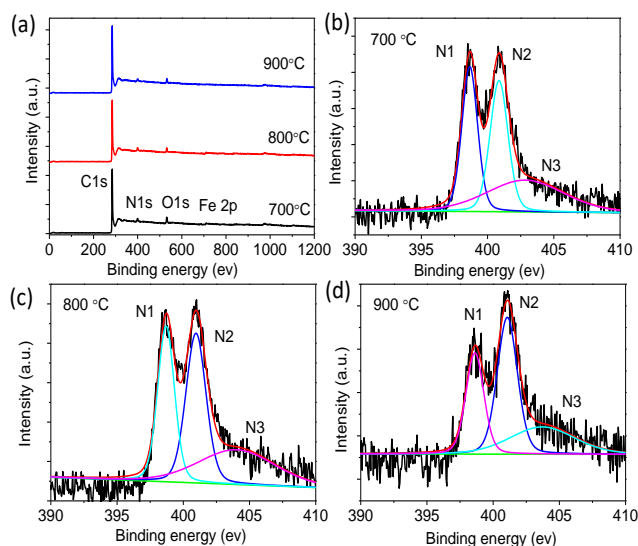

Fig. 4. XPS survey spectrum (a) and the high-resolution XPS spectra of N 1s, (b-d) pyrolyzed 11.54% Fe composites synthesized at different temperatures.

As shown in **Table 1**, for pyrolyzed samples, the content of N1 (Fe-Nx, most likely in the form of Fe_3N) increased to a maximum value at the temperature of 700 °C, which is consistent with the XRD result. Recently, some reports have demonstrated that high proportion of pyridinic N can increase current density, spin density and the density of π states of the C atoms near the Fermi level, thus boosting the O_2 reduction [16, 17].

Table 1. Percentage content of different N species in total N amount for G/dots/Fe-Nx, calculated from the N 1s data of XPS.

Annealing Temperature	Total N atomic %	N1 Fe−Nx (%)	N2 quaternary (%)	N3 oxidized N (%)
700 ℃	5.3	32.2	33.3	34.5
800 ℃	4.7	31.5	36.4	32.1
900 ℃	3.5	28.7	43.6	27.7

Electrocatalytic performances of the hybridized materials were investigated with cyclic voltammetry (CV) measurements in a N_2- and O_2-saturated 0.1 M KOH solution at a scan rate of 50 mVs⁻¹. As presented in **Fig. 5a**, featureless CV plots were observed for all four samples in N_2- saturated KOH electrolyte, whereas a single cathodic reduction peak centered at 0.683 V, 0.744 V, 0.742 V, 0.701V (vs RHE) can be identified in O_2-saturated solution, corresponding to samples obtained at different calcination conditions, respectively, which indicates that all samples exhibited catalytic activity toward ORR.

Fig. 5b shows the RDE voltammograms in O_2-saturated 0.1 M KOH at room temperature (rotation speed 1600 rpm, sweep rate 10 mVs⁻¹). It is shown that the annealing

temperature has a great impact on the ORR catalytic activity. With ramping the annealing temperature from 600 to 900 °C, the ORR kinetic currents show the two-stage fluctuation, as the current first increased from 600 °C and reached a maximum at 700 °C with a half-wave potential of 0.753 V vs RHE, then decrease from 800 to 900 °C. The ORR half-wave potential for the G/dots/Fe_3N (700 °C) is only 57 mV less than that of the commercial Pt/C catalyst (0.810 V vs RHE) (Fig. S2). Importantly, the G/dots/Fe_3N (700 ℃) catalyst exhibits larger current density than that of commercial Pt/C, indicating that the electrode exhibits preferred catalytic activities.
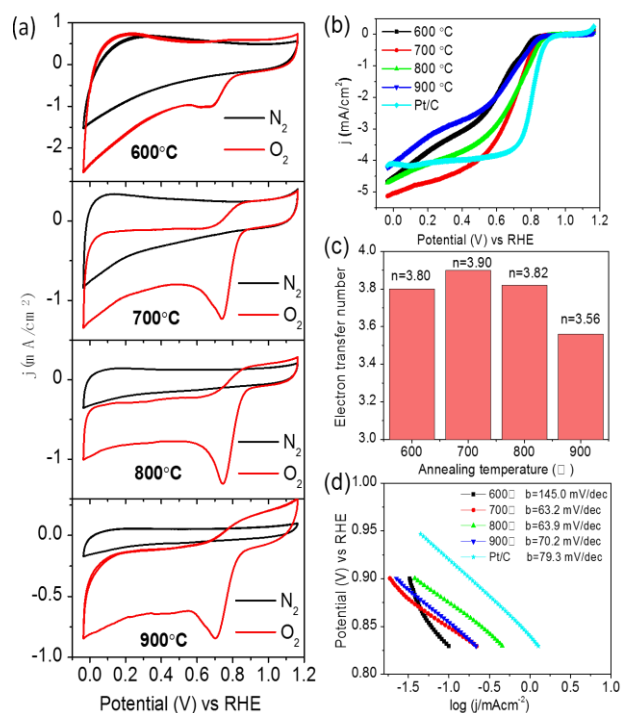

Fig. 5. (a) CV curves of as-prepared samples obtained under different calcination conditions in N_2- and O_2-saturated 0.1 M KOH at a scan rate of 50 mV s⁻¹ (b) Linear sweep voltammetric (LSV) curves of as-prepared samples in O_2-saturated 0.1 M KOH at a scan rate of 10 mV s⁻¹, rotation rate = 1600 rpm. (c) Electron transfer number of as-prepared samples at 0.3 V-0.6 V (d) Tafel ORR plots for the as-prepared samples and Pt/C.

Fig. 5c displays the electron transfer number (*n*) of the composites synthesized at different temperatures (calculated from **Fig. S4**). It is clear that G/dots/Fe_3N (700 ℃) displays the optimal catalytic activity with the highest electron transfer number of 3.90, which is much higher than the others. The Tafel slope was also calculated to evaluate the ORR kinetic characteristics of the composites pyrolyzed at different temperatures and Pt/C (**Fig. 5d**). Kinetic currents (**Fig. 5d**) derived from **Fig. 5b** show a Tafel slope of 145.0, 63.2, 63.9, 70.2 mV dec⁻¹ of catalysts obtained at different calcination conditions (600-900°C), respectively. Those data are close to the Pt/C catalyst (79.3 mV dec⁻¹) except for composite synthesized at 600 ℃. The relatively low Tafel slope demonstrated the relatively high intrinsic catalytic activity of G/dots/Fe_3N. Generally, a low Tafel slope indicates a high intrinsic exchange current density (i.e., a high reaction rate) [18, 19].
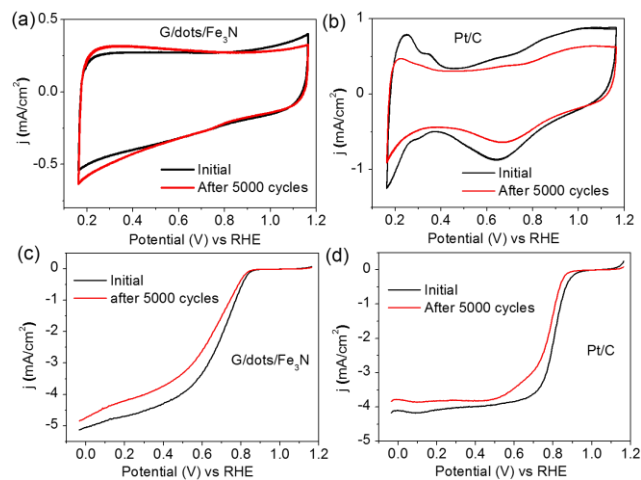
Fig. 6. CV curve comparisons in N_2-saturated 0.1 M KOH solution with 5000 cycles of (a) G/dots/Fe$_3$N; (b) commercial Pt/C. Scan rate: 50 mV s^{-1}. LSV curves of (c) G/dots/Fe$_3$N and (d) Pt/C for ORR in O_2-saturated 0.10 M KOH before and after 5000 cycles. Scan rate: 10 mV s^{-1}, rotation rate = 1600 rpm.

The cyclic stability of catalysts was measured by continuously cycled the sample from 0.6 to 1.0 V with a scan rate of 50 mV s^{-1} in O_2-saturated 0.1 M KOH for 5000 cycles. The ORR LSV curves of G/dots/Fe$_3$N (700 °C) and Pt/C (20 μg- cm^{-2}) before and after 5000 cycles were shown in **Fig. 6c and d**, respectively. There was a 56 mV loss of half-wave potential for G/dots/Fe$_3$N catalyst (**Fig. 6c**) while a 34 mV loss for the Pt/C catalyst under the same conditions (**Fig. 6d**), indicating a comparable cyclic stability with commercial Pt/C.
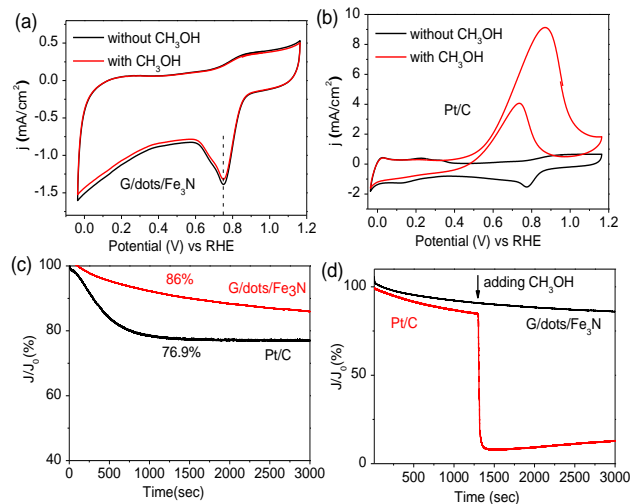
Fig.7. CVs of the (a) G/dots/Fe$_3$N and (b) Pt/C in O_2-saturated 0.10 M KOH with and without10% CH$_3$OH. Scan rate: 50 mV s^{-1}. Chronoamperometric responses of G/dots/Fe$_3$N, Pt/C at 0.664 V (vs RHE) in 0.1 M KOH, (c) without and (d) with adding 10% CH$_3$OH, rotation rate = 1600 rpm.

Furthermore, the tolerance toward methanol of the G/dots/Fe$_3$N and Pt/C catalyst were determined upon addition of 10%V methanol into 0.10 M KOH electrolyte. **Fig. 7a** shows that there are almost no changes in the cathodic reduction peak current for the G/dots/Fe$_3$N after the addition of methanol. However, the Pt/C catalyst shows the typical inverse methanol oxidation peaks in CVs (**Fig. 7b**). These results suggest that G/dots/Fe$_3$N has

much better catalytic selectivity toward ORR than the commercial Pt/C catalyst. Stability of the G/dots/Fe$_3$N electrode was also tested under a constant potential of 0.664 V (vs RHE) in O_2-sturated 0.1 M KOH at an electrode rotation rate of 1600 rpm. As shown in **Fig. 7c**, the G/dots/Fe$_3$N electrode exhibited an excellent durability with only about 14% attenuation in current after 3000 s. For comparison, 20% Pt/C catalyst was also tested under the same condition and showed a more pronounced attenuation (∼23%, **Fig. 7c**). In addition, **Fig. 7d** shows that there is almost no current change for the G/dots/Fe$_3$N after the addition of methanol. In contrast, Pt/C catalyst showed a drastic decrease (∼90%, **Fig. 7d**) once methanol was added. This result further illustrates that the catalyst not only has a better durability than Pt/C but also exhibits a higher selectivity for ORR combined with excellent tolerance to methanol poisoning effects.

Conclusion

In summary, we have successfully synthesized a new kind of nanohybrid of porous graphene flakes, dots and Fe$_3$N nanocrystals through electrochemically charging/ discharging of graphite in ionic liquid/water followed by thermal annealing at the presence of FeCl$_3$. The phase of material, the active sites, and electrical conductivity could be tunable. Rich edges of graphene dots and porous flakes with heteroatom-doping could supply sufficient active sites and good pathway for electrons/ions/gases for ORR. This material exhibited high electrolytic performance, excellent tolerance to methanol and superior stability in alkaline solutions. We expect that this kind of graphene hybrid synthesized from graphite could be developed as a good candidate for a non-precious metal catalyst in metal-air batteries and fuel cells.

Supporting information

Supporting Information Available: Additional experimental details and SEM, TEM, XPS, TGA characterization. This material is available free of charge via the Internet at http.

References

1. Wei, W.; Liang, H.; Parvez, K.; Zhuang, X.; Feng, X.; Müllen, K.; *Angew. Chem.*, **2014**, 126, 1596.
   DOI: 10.1002/ange.201307319
2. Liu, Y.; Mustain Y.; *J. Am. Chem. Soc*., **2013**, 135, 530.
   DOI: 10.1021/ja307635r
3. Steele, B.; Heinzel, A.; *Nature*, **2001**, 414, 345.
   DOI: 10.1038/35104620
4. Escaoño, M.; *Nano Research*, **2015**, 8, 1689.
   DOI: 10.1007/s12274-014-0670-1
5. Tan, X.; Prabhudev, S.; Kohandehghan, A.; Karpuzov, D.; Botton, G.; Mitlin, D.; *ACS Catal*., **2015**, 5, 1513.
   DOI: 10.1021/cs501710b
6. Devivaraprasad, R.; Ramesh, R.; Naresh, N.; Kar, T.; Singh, R.; Neergat, M.; Langmuir, 2014, 30, 8995.
   DOI: 10.1021/la501109g
7. Lin, L.; Zhu, Q.; Xu, A.; *J. Am. Chem. Soc*., **2014**, 136, 11027.
   DOI: 10.1021/ja504696r

8. Lai, Q.; Su, Q.; Gao, Q.; Liang, Y.; Wang, Y.; Yang, Z.; Zhang, X.; He, J.; Tong, H.; *ACS Appl. Mater. Interfaces*., **2015**, 7, 18170.
    DOI: 10.1021/acsami.5b05834
9. Li, R.; Wei, Z.; Gou, X.; *ACS Catal.* **2015**, 5, 4133.
    DOI: 10.1021/acscatal.5b00601
10. Gong, Y.; Fei, H.; Zou, X.; Zhou, W.; Yang, S.; Ye. G.; Liu, Z.; Peng, Z.; Lou, J.; Vajtai, R.; Yakobson, B.; Tour, J.; *Chem. Mater*., **2015**, 27, 1181.
    DOI: 10.1021/cm5037502
11. Yang, W.; Liu, X.; Yue, X.; Jia, J.; Guo, S.; *J. Am. Chem. Soc*., 2015, 137, 1436.
    DOI: 10.1021/ja5129132
12. Singh, K.; Bae, E.; Yu, J.; *J. Am. Chem. Soc*., **2015**, 137, 3165.
    DOI: 10.1021/ja511759u
13. Jiang, H.; Yao, Y.; Zhu, Y.; Liu, Y.; Su, Y.; Yang, X.; Li, C.; *ACS Appl. Mater. Interfaces*., **2015**, 7, 21511.
    DOI: 10.1021/acsami.5b06708
14. Chen, L.; Xiao, J.; Liu, B.; Yi, T.; *ACS Appl. Mater. Interfaces*., **2016**, 8, 16649.
    DOI: 10.1021/acsami.6b02522
15. Lin, L.; Yang, Z.; Jiang, Y.; Xu, A.; ACS Catal.; 2016, 6, 4449.
    DOI: 10.1021/acscatal.6b00535
16. Liang, J.; Jiao, Y.; Jaroniec, M.; Qiao, S.; *Angew. Chem. Int. Ed.,* **2012**, 51, 11496.
    DOI: 10.1002/anie.201206720
17. Luo, Z.; Lim, S.; Tian, Z.; Shang, J.; Lai, L.; MacDonald, B.; Fu, C.; Shen, Z.; Yu, T.; Lin, J.; *J. Mater. Chem.*, **2011**, 21, 8038.
    DOI: 10.1039/C1JM10845J
18. Wu, G.; More, K.; Johnston, C.; Zelenay, P.; *Science*, **2011**, 332, 443.
    DOI: 10.1126/science.1200832
19. Jiao, Y.; Zheng, Y.; Jaroniec, M.; Qiao, S.; *J. Am. Chem. Soc*., **2014**, 136, 4394.
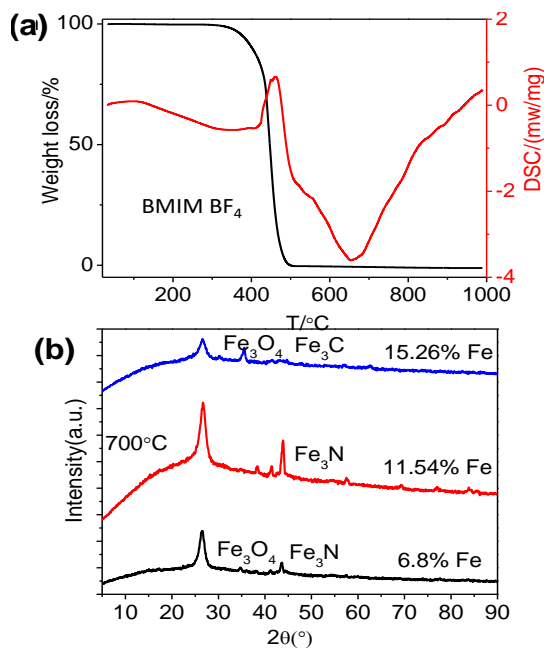   **DOI:** 10.1021/ja500432h

Supporting Information

Fig. S1. (a) TGA curve (in Ar atmosphere) of ionic liquid [BMIM][BF$_4$], (b) XRD patterns of graphene flakes/dots/Fe$_3$N obtained by annealing at 700ºC.
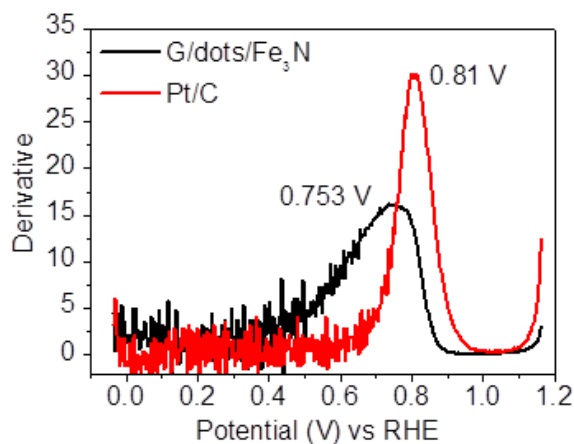

Fig. S2. The half potential of G/dots/Fe$_3$N compared with that of the commercial Pt/C.
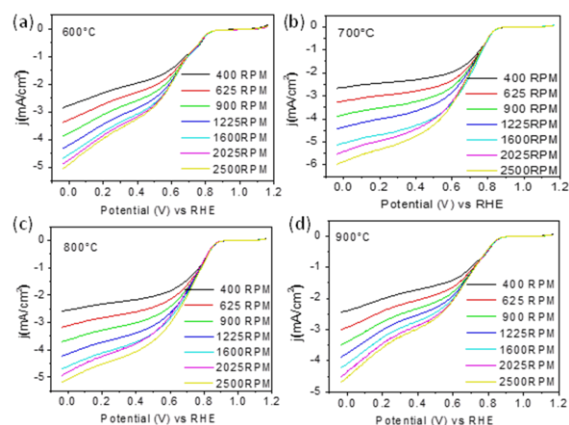

Fig. S3. (a-d) RDE LSV of ORR on G/dots/Fe$_3$X (annealing at different temperatures) electrodes at different rotating speeds in an O$_2$-saturated 0.1 M KOH solution with a scan rate of 10 mV s^{-1}.
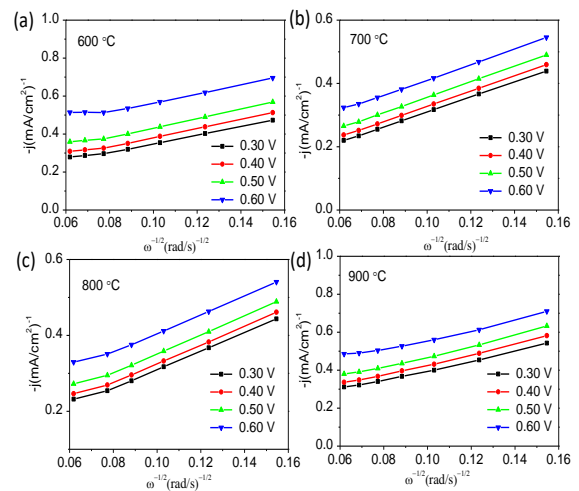

Fig. S4. (a-d) K−L plots of G/dots/Fe$_3$X (annealing at different temperatures) derived from RDE LSV at different potentials
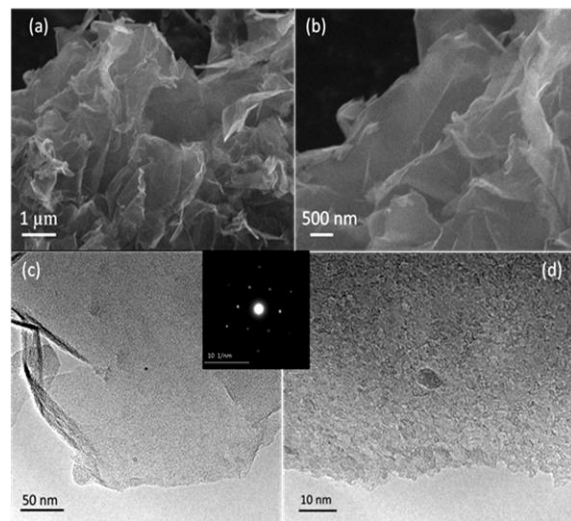

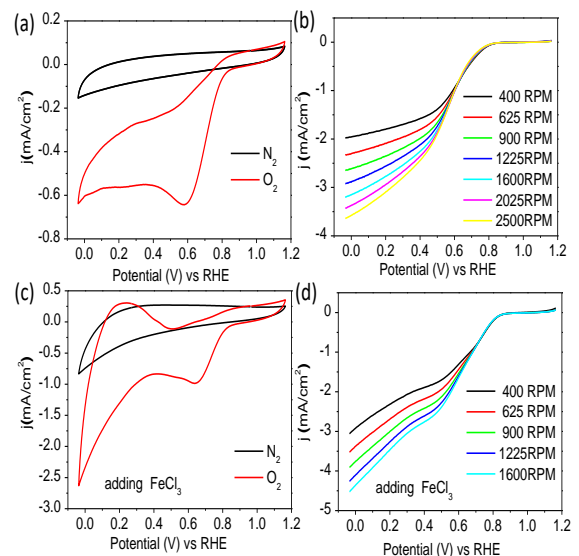**Fig. S5**. SEM and TEM images of G/dots (700 ºC)

Fig. S7. (a, b) CV and LSV curves of ionic liquid ([BMIM][BF$_4$]) annealing at 700 ºC (G/dots), (c, d) CV and LSV curves of ionic liquid ([BMIM][BF$_4$]) adding FeCl$_3$ (C/Fe$_3$N) annealing at 700 ºC.
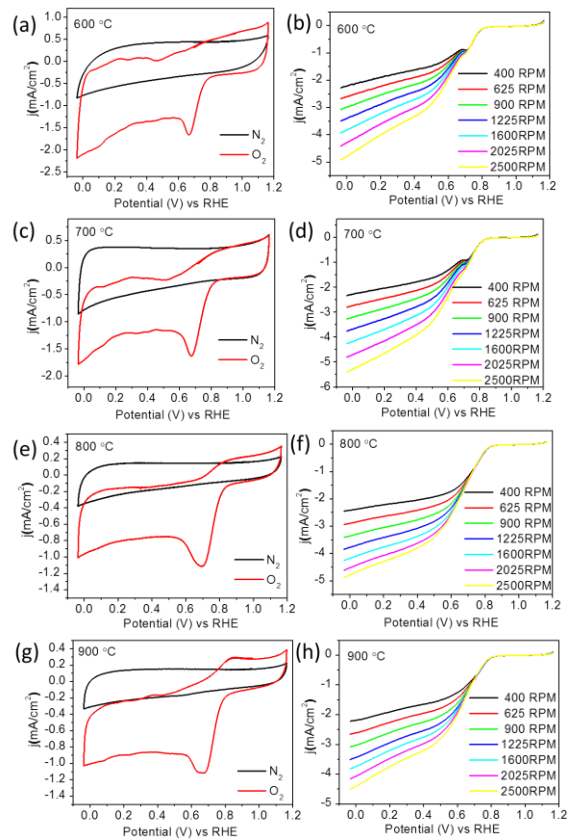
Fig. S8. (a-h) CV and LSV curves of G/dots annealing at different temperatures (600-900 ℃)